Theor Chem Acc (2006) 116: 404–419
DOI 10.1007/s00214-006-0092-6

REGULAR ARTICLE

A.J.C. Varandas · L.A. Poveda

Accurate DMBE potential energy surface for the $N(^2D) + H_2(^1\Sigma_g^+)$ reaction using an improved switching function formalism

Received: 4 November 2004 / Accepted: 8 March 2005 / Published online: 23 March 2006

Abstract A single-sheeted double many-body expansion (DMBE) potential energy surface is reported for the $1\,^2A''$ state of NH_2. To approximate its true multi-sheeted nature, a novel switching function that imposes the correct behavior at the $H_2(X\,^1\Sigma_g^+)$+ $N(^2D)$ and $NH(X\,^3\Sigma^-)$ + $H(^2S)$ dissociation limits has been suggested. The new DMBE form is shown to fit with high accuracy an extensive set of new ab initio points (calculated at the multi-reference configuration interaction level using the full valence complete active space as reference and aug-cc-pVQZ and aug-cc-pV5Z basis sets) that have been semiempirically corrected at the valence regions by scaling the n-body dynamical correlation terms such as to account for the finite basis set size and truncated configuration interaction expansion. A detailed study of the $N(^2D)\cdots H_2(X\,^1\Sigma_g^+)$ van der Waals region has also been carried out. These calculations predict a nearly free rigid-rotor with two shallow van der Waals wells of C_{2v} and $C_{\infty v}$ symmetries. Such a result contrasts with previous cc-pVTZ calculations which predict a single T-shaped van der Waals structure. Except in the vicinity of the crossing seam, which is replaced by an avoided intersection, the fit shows the correct physical behavior over the entire configurational space. The topographical features of the new DMBE potential energy surface are examined in detail and compared with those of other potential functions available in the literature. Amongst such features, we highlight the barrier for linearization ($11,802\,cm^{-1}$) which is found to overestimate the most recent empirical spectroscopic estimate by only $28\,cm^{-1}$. Additionally, the T-shaped $N(^2D)\cdots H_2$ van der Waals minimum is predicted to have a well depth of $90\,cm^{-1}$, being $11\,cm^{-1}$ deeper than the $C_{\infty v}$ minimum. The title DMBE form is therefore recommendable for dynamics studies of both non-reactive and reactive $N(^2D) + H_2$ collisions.

A.J.C. Varandas (✉) · L.A. Poveda
Departamento de Química,
Universidade de Coimbra,
Coimbra, 3004-535 Portugal
E-mail: varandas@qtvs1.qui.uc.pt

1 Introduction

The $N(^4S,^2D,^2P)+H_2$ reaction has been the subject of considerable theoretical and experimental work due to the fundamental importance of nitrogen reactivity in atmospheric chemistry and combustion processes. Since the ground state nitrogen atoms, $N(^4S)$, are often not very reactive, a major interest has been focused on reactions involving their lowest $N(^2D)$ excited state.

During the past decade, the $N(^2D) + H_2(X\,^1\Sigma_g^+) \rightarrow NH(X\,^3\Sigma^-)+H(^2S)$ reaction has been studied using a LEPS (London–Eyring–Polanyi–Sato) potential energy surface proposed by Suzuki et al. [1], and a more realistic form obtained by fitting ab initio data to a Sorbie–Murrell type function [2]. Both theoretical studies concluded that the collinear (abstraction) path is dominant in the $N(^2D)+H_2(^1\Sigma_g^+)$ reaction, in agreement with a previous experimental result which provides evidence that it proceeds via a direct hydrogen atom abstraction mechanism [3]. However, more recent experimental results based on induced fluorescence [4,5] and crossed molecular beam studies [6] suggest an insertion mechanism for the title reaction. Such a controversy has recently been clarified by using a global potential energy surface for the $1\,^2A''$ state of NH_2 reported by Ho et al. [37]. This surface, obtained by using the reproducing Kernel Hilbert Space (RKHS) interpolation method [8–10], represents an improved version of a previous RKHS surface [11] modeled from a fit to high quality ab initio data. Both these potential energy surfaces predict the $N(^2D) + H_2(^1\Sigma_g^+) \rightarrow NH(X\,^3\Sigma^-)+H(^2S)$ reaction to proceed via a perpendicular approach of the nitrogen atom to H_2. In fact, quasiclassical trajectory (QCT) calculations based on such potential energy surfaces show excellent agreement with the more recent experimental measurements. There have been other ab initio potential energy surfaces for the title system. Of these, we mention the surfaces of Buenker et al. [12] and Gabriel et al. [13] for both the $\tilde{X}$ and $\tilde{A}$ states of the bent–bent Renner–Teller NH_2 system. In fact, additionally to the ab initio data, Gabriel et al. [13] carried out fits to their own

data with a view to analyze the $\tilde{A}\,^2A_1 - \tilde{X}^2B_1$ spectrum, having achieved a high accuracy. They report a barrier height of $11,914\,\mathrm{cm}^{-1}$ for the linearization of $NH_2(\tilde{X}\,^2B_1)$, although a more recent estimate [14] based on an empirically calibrated stretch-bender model points to a slightly lower value of $11,774\,\mathrm{cm}^{-1}$.

In this work, we report a realistic global potential energy surface for $NH_2(1\,^2A'')$ based on double many-body expansion (DMBE) [15–17] theory. Corresponding to a possible fragment of larger N_xH_y species such as those of relevance in studying the synthesis of ammonia, it may therefore play a key role in the construction of global DMBE forms for such polyatomic systems. Indeed, this has been a primary motivation for modeling an accurate single-sheeted DMBE potential energy surface for the title system.

To warrant that the potential energy surface dissociates to the correct asymptotes, we make use of an improved switching function approach [18]. In turn, the calibration employed 1,498 ab initio points calculated at the multi-reference configuration interaction (MRCI) level using the full valence complete active space (FVCAS) as the reference function and the augmented polarized quadruple zeta (aug-cc-pVQZ or AVQZ) basis set of Dunning [19,20]. To extrapolate the ab initio energies to the complete basis set/complete CI limit, they have been corrected semiempirically by using the double many-body expansion–scaled external correlation (DMBE-SEC) [21] method. As usual in DMBE [15–17] theory, the potential energy surface so obtained shows the correct long-range behavior at the dissociation channels while providing a realistic representation at all interatomic separations. For further realism, additional calculations of the long range $N(^2D)+H_2(^1\Sigma_g^+)$ interaction have been carried using a computationally more demanding aug-cc-pV5Z (AV5Z) basis set [19,20], which were too corrected semiempirically by using the DMBE–SEC method.

The paper is organized as follows. Section 2 describes the ab initio calculations carried out in the present work, while Sect. 3 focuses on their modeling using DMBE theory. Specifically, Sect. 3.1 focuses on the two-body energy terms, and Sect. 3.2 in the three-body ones. The major topographical features of the DMBE potential energy surface are examined in Sect. 4. Sect. 5 gathers the concluding remarks.

2 Ab initio calculations

The ab initio calulations have been carried out at the MRCI [22] level using the FVCAS [23] wave function as reference. This involves seven correlated electrons in six active orbitals ($5a' + 1a''$), amounting to a total of 50 configuration state functions. The AVQZ atomic basis set of Dunning [19,20] has been employed, and the calculations carried out using the MOLPRO [24] package. To map the potential energy surface, a total of 1,532 points have been calculated (34 estimated from nearby points through interpolation) over $N - H_2$ regions defined by $1 \le R_{H_2}/a_0 \le 3.5$, $1 \le r_{N-H_2}/a_0 \le 11$, and $0° \le \gamma \le 90°$ while, for $H - NH$, they cover geometries defined by $1.5 \le R_{NH}/a_0 \le 3.5$, $1 \le r_{H-NH}/a_0 \le 10$, and $0° \le \gamma \le 180°$; R, r, and γ are the atom–diatom Jacobi coordinates. For improved accuracy, 44 of the above ab initio points have been calculated using the AV5Z basis set [19,20] for geometries encompassing the $N-H_2$ van der Waals minimum: $R_{H_2} = 1.2, 1.401, 1.6\,a_0$, $5.5 \le r_{N-H_2}/a_0 \le 8.0$, and $\gamma = 4°,\ 8°,\ 15°,\ 30°,\ 45°,\ 60°,\ 75°$.

To account for electronic excitations beyond singles and doubles and, most importantly, for the incompleteness of the basis set, the calculated ab initio energies have been semiempirically corrected using the DMBE–SEC [25] method. Accordingly, the total DMBE–SEC interaction energy is written as

$$V(\mathbf{R}) = V_{FVCAS}(\mathbf{R}) + V_{SEC}(\mathbf{R}) \tag{1}$$

where

$$V_{FVCAS}(\mathbf{R}) = \sum_{AB} V^{(2)}_{AB,FVCAS}(R_{AB}) + V^{(3)}_{ABC,FVCAS}(\mathbf{R}) \tag{2}$$

$$V_{SEC}(\mathbf{R}) = \sum_{AB} V^{(2)}_{AB,SEC}(R_{AB}) + V^{(3)}_{ABC,SEC}(\mathbf{R}) \tag{3}$$

and $\mathbf{R} = \{R_{AB}, R_{BC}, R_{AC}\}$ is a collective variable of all internuclear distances (these are equivalently denoted as $\{R_i\}$, with $i = 1-3$). Explicitly, the first two terms of the DMBE–SEC series expansion assume the form:

$$V^{(2)}_{AB,SEC}(R_{AB}) = \frac{V^{(2)}_{AB,FVCAS-CISD}(R_{AB}) - V^{(2)}_{AB,FVCAS}(R_{AB})}{F^{(2)}_{AB}} \tag{4}$$

$$V^{(3)}_{ABC,SEC}(\mathbf{R}) = \frac{V^{(3)}_{ABC,FVCAS-CISD}(\mathbf{R}) - V^{(3)}_{ABC,FVCAS}(\mathbf{R})}{F^{(3)}_{ABC}} \tag{5}$$

Following previous work [25], the $F^{(2)}_{AB}$ parameter in Eq. (4) has been chosen to reproduce the bond dissociation energy of the corresponding AB diatomic. Rather than choosing $F^{(3)}_{ABC}$ to mimic the empirical well depth of $NH_2(\tilde{X}\,^2B_1)$ which is somewhat uncertain ($124.5 \pm 0.2\,\mathrm{kcal\,mol}^{-1}$; the error bar has been taken from the reported heat of formation [26]), we have instead fixed $F^{(3)}_{ABC}$ at the average of the 3 two-body F-factors. For the AVQZ basis set, such a procedure leads to $F^{(2)}_{HH} = 0.9773$, $F^{(2)}_{NH} = 0.9479$, and $F^{(3)}_{NHH} = 0.9577$. In turn, for the AV5Z basis set, the scaling factors are $F^{(2)}_{HH} = 0.9904$, $F^{(2)}_{NH} = 0.9786$, and $F^{(3)}_{NHH} = 0.9825$. Since our MRCI energies have been extrapolated to the complete basis set/configuration interaction limit, we judged it unnecessary to correct the results for the basis set superposition error [27].

3 Single-sheeted potential energy surface

An approximate representation of a multi-sheeted potential energy surface by a single-sheeted form involves necessarily the use of switching functions. Such a procedure has first

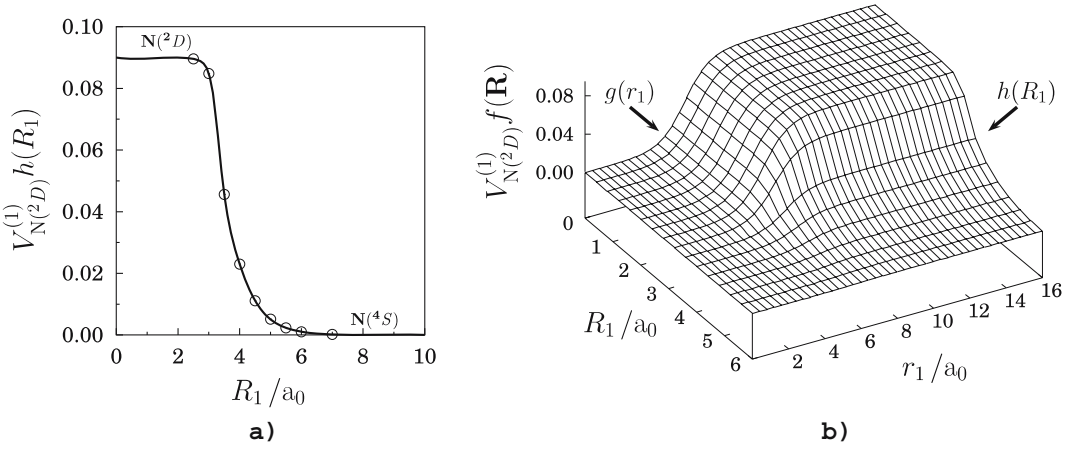

Fig. 1 Switching function used to model the single-sheeted NH_2 double many-body expansion (DMBE) potential energy surface. Shown in the *left panel* is the fit of the $h(R_1)$ switching form to the ab initio points calculated for $N + H_2$ configurations as a function of the H–H distance (R_1). Shown in the *right-hand side panel* is a perspective view of the global switching function in Eq. (11)

been proposed by Murrell and Carter [18], who applied it in the construction of an approximate potential energy surface for the ground-state of H_2O. In their paper, they have employed the switching function

$$f(\mathbf{R}) = \frac{1}{2}\{1 - \tanh[(3\rho_3 - \rho_1 - \rho_2)(\alpha/2)]\} \tag{6}$$

where $\rho_i = R_i - R_i^0$ are the displacements from a reference geometry (R_3 is the $H - H$ distance, R_1 and R_2 the $O - H$ ones), and α is a range-determining parameter. Such a function allows the $O(^1D)$ state to appear in the $O(^1D)+H_2(^1\Sigma_g^+)$ channel (*i.e.*, for $\rho_1, \rho_2 \to \infty$) while being absent in the $OH(^2\Pi) + H(^2S)$ channel ($\rho_3 \to \infty$). A similar situation holds for the title system, where the following dissociation scheme applies:

$$NH_2(1\,^2A'') \to H_2(X\,^1\Sigma_g^+) + N(^2D), \tag{7}$$

$$\to NH(X\,^3\Sigma^-) + H(^2S). \tag{8}$$

Since $NH(^3\Sigma^-)$ dissociates to ground-state atoms, it is necessary to introduce a function that removes the $N(^2D)$ state from this channel. However, as noted in [18], the function (6) cannot reach a unique value at the three-atom limit. Such an inconsistency prompted us to develop a more realistic switching function. We suggest the form

$$h(R_1) = \frac{1}{4}\sum_{i=1}^{2}\{1 - \tanh[\alpha_i(R_1 - R_1^{i0}) + \beta_i(R_1 - R_1^{i1})^3]\} \tag{9}$$

where R_1 represents the $H - H$ distance, and α_i and β_i ($i = 1, 2$) are parameters to be calibrated from a least-squares fit to an extra set of 15 AVQZ points that control the $N(^2D) - N(^4S)$ decay as the $H - H$ distance increases for $N + H_2$ configurations (see the left-hand-side panel of Fig. 1). As a check to the fit, we observe that at $R_1 = 1.401$ a_0 the switching function differs by less than 10^{-6} from unit, thus warranting the correct energetics at the $N(^2D) + H_2(X\,^1\Sigma_g^+)$ asymptote.

To get a smooth three-body energy term, we further suggest to multiply Eq. (9) by an amplitude function that annihilates Eq. (9) at short-range regions (short $N - H_2$ distances):

$$g(r_1) = \frac{1}{2}\{1 + \tanh[\alpha(r_1 - r_1^0)]\} \tag{10}$$

where r_1 is the distance of the N atom to the center of mass of H_2. A word is necessary at this point to clarify the notation. If the indexes (i, j, k) number the atoms (say, 1 for N, and 2 and 3 for H), r_i represents the Jacobi coordinate separating atom i from the center of mass of diatom jk whose bond distance is itself denoted by R_i. The final switching function then assumes the form

$$f(\mathbf{R}) = g(r_1)h(R_1) \tag{11}$$

with the parameters of $g(r_1)$ being chosen such as to warrant that its main effect occurs for $N - H_2$ distances larger than 8 a_0 or so (see the right-hand side panel of Fig. 1). The numerical values of all parameters in Eq. (11) are collected in Table 1.

Table 1 Parameters in the switching function of Eq. (11)

Parameter	Numerical value
α_1	0.718244
α_2	0.719351
β_1	0.493967
β_2	0.066742
R_1^{10}	2.417270
R_1^{11}	4.355230
R_1^{20}	3.435560
R_1^{21}	5.520390
α	0.75
r_1^0	5.5

Within the framework of DMBE theory, the single-sheeted potential energy surface is written as

$$V(\mathbf{R}) = V^{(1)}_{\mathrm{N}(^2D)} f(\mathbf{R}) + \sum_{i=1}^{3} [V^{(2)}_{\mathrm{EHF}}(R_i) + V^{(2)}_{\mathrm{dc}}(R_i)] + [V^{(3)}_{\mathrm{EHF}}(\mathbf{R}) + V^{(3)}_{\mathrm{dc}}(\mathbf{R})] \quad (12)$$

where $V^{(1)}_{\mathrm{N}(^2D)}$ represents the difference in energy (at the scaled AVQZ level) between the ^2D and ^4S states of atomic nitrogen: $V^{(1)}_{\mathrm{N}(^2D)} = 0.09014\,\mathrm{E_h}$. For simplicity, we denote the resulting DMBE potential energy surface by $V(\mathbf{R})$, although this should not be confused with the scaled ab initio energies calculated in Eq. (1) which are used to calibrate Eq. (12). The following sections give the details of the analytical forms employed to represent the various energy terms in the latter.

3.1 Two-body energy terms

The potential energy curves for the two-body fragments are based on the extended Hartree–Fock approximate correlation energy method for diatomic molecules including the united atom limit [28] (EHFACE2U) which show the correct behavior at both the asymptotic limits $R \to 0$ and $R \to \infty$. They are given by the sum of two terms: (a) the extended-Hartree-Fock energy:

$$V_{\mathrm{EHF}}(R) = -\frac{D}{R}\left(1 + \sum_{i=1}^{n} a_i r^i\right)\exp(-\gamma r) \quad (13)$$

where r (without any subscript) denotes the displacement coordinate relative to the equilibrium geometry of the diatomic, $r = R - R_e$; (b) the dynamical correlation energy:

$$V_{\mathrm{dc}}(R) = -\sum_{n=6,8,10} C_n \chi_n(R) R^{-n} \quad (14)$$

where

$$\gamma = \gamma_0\left[1 + \gamma_1 \tanh(\gamma_2 r)\right] \quad (15)$$

and

$$\chi_n(R) = \left[1 - \exp\left(-A_n\frac{R}{\rho} - B_n\frac{R^2}{\rho^2}\right)\right]^n \quad (16)$$

is a charge-overlap damping function for the long-range dispersion energy (as well as the electrostatic and induction energies, in case these must be considered). In turn, $A_n = \alpha_0 n^{-\alpha_1}$ and $B_n = \beta_0 \exp(-\beta_1 n)$ are auxiliary functions [15, 29]; $\alpha_0 = 16.36606$, $\alpha_1 = 0.70172$, $\beta_0 = 17.19338$, and $\beta_1 = 0.09574$. Moreover, $\rho = 5.5 + 1.25R_0$ is a scaling parameter, $R_0 = 2(\langle r_{\mathrm{A}}^2\rangle^{\frac{1}{2}} + \langle r_{\mathrm{B}}^2\rangle^{\frac{1}{2}})$ is the LeRoy [30] parameter for the onset of the undamped R^{-n} expansion, and $\langle r_{\mathrm{X}}^2\rangle$ is the expectation value of the squared radius for the outermost electrons of atom X (X = A, B). Finally, D and $a_i (i = 1, \ldots, n)$ in Eq. (13) are adjustable parameters to be obtained as described elsewhere [15,28]. Here, we employ the accurate EHFACE2U potential energy curve of ground-state $H_2(X^1\Sigma_g^+)$ reported in [31], and the curve of ground-state imidogen, $NH(X^3\Sigma^-)$, modeled [32] from MRCI+Q ab initio points [33]. As shown in Fig. 2, both potential curves mimic accurately the ab initio energies calculated in the present work, being for completeness numerically defined in Table 2.

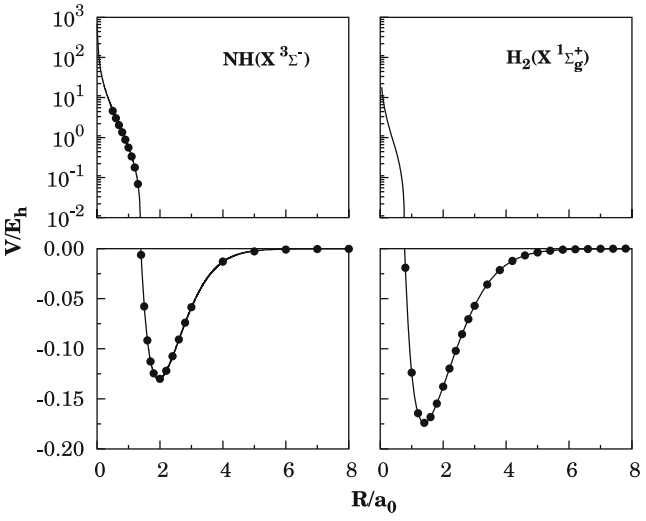

Fig. 2 EHFACE2U potential energy curves for $NH(X^3\Sigma^-)$ and $H_2(X^1\Sigma_g^+)$. The *solid dots* indicate the multi-reference configuration interaction (MRCI) points calculated in the present work

Table 2 Parameters of two-body potential energy curves in Eqs. (13)–(16)

	$NH(X^3\Sigma^-)$	$H_2(X^1\Sigma_g^+)$
R_e/a_0	1.9650	1.401
D/E_h	0.22903401	0.22979439
a_1/a_0^{-1}	2.14664173	1.82027480
a_2/a_0^{-2}	0.84471252	0.52437767
a_3/a_0^{-3}	0.52590829	0.36999610
γ_0/a_0^{-1}	1.563792	1.094670
γ_1/a_0^{-1}	0.661116	1.009737
γ_2/a_0^{-1}	0.282985	0.235856
$A/E_h a_0^{-\tilde{\alpha}}$		−0.8205
$\tilde{a}_1/a_0^{-1}$		0
$\tilde{\alpha}$		2.5
$\tilde{\gamma}/a_0^{-1}$		2.0
R_0/a_0	6.6570	6.9282
$C_6/E_h a_0^{-6}$	12.27	6.499
$C_8/E_h a_0^{-8}$	232.6	124.4
$C_{10}/E_h a_0^{-10}$	5,775	3286.0
$C_{11}/E_h a_0^{-11}$		−3475
$C_{12}/E_h a_0^{-12}$		121,500
$C_{13}/E_h a_0^{-13}$		−291,400
$C_{14}/E_h a_0^{-14}$		6,061,000
$C_{15}/E_h a_0^{-15}$		−23,050,000
$C_{16}/E_h a_0^{-16}$		393,800,000

Table 3 Numerical values of the parameters in Eq. (19)

	$C_6^0(R)$	$C_6^2(R)$	$C_8^0(R)$	$C_8^2(R)$	$C_8^4(R)$	$C_{10}^0(R)$
$N-H_2$						
R_M/a_0	3.4158	3.2065	3.1636	3.0873	3.0865	2.9727
D_M/E_h	5.9304	3.7795	270.9628	368.8294	28.4794	12092.994
a_1/a_0^{-1}	1.20680520	0.48898303	0.665 91220	0.76028418	0.83439744	0.48401110
a_2/a_0^{-2}	0.37773924	0.01948220	0.11981357	0.16713192	0.21372145	0.10838466
a_3/a_0^{-3}	0.04733974	−0.01028989	0.05013767	0.00786882	0.01482201	0.06850918
b_2/a_0^{-2}	0.20828895	0.23889466	0.23466806	0.24666219	0.50597119	0.25442128
b_3/a_0^{-3}	2.7×10^{-9}	2.4×10^{-9}	5.4×10^{-10}	1.2×10^{-8}	6.9×10^{-9}	7.9×10^{-9}
$H-NH$						
R_M/a_0	3.4400	3.2341	3.5037	3.2923	3.2491	3.5428
D_M/E_h	3.3090	3.0188	57.5906	183.9318	14.6299	1311.7401
a_1/a_0^{-1}	1.63305447	0.57469334	1.805 549 07	1.06820652	1.23496592	0.83907020
a_2/a_0^{-2}	0.75223477	0.03086175	0.79931630	0.32533177	0.34210854	−1.10009919
a_3/a_0^{-3}	0.11845516	0.04274567	0.13285442	0.02961379	−0.02301909	−0.24807000
b_2/a_0^{-2}	0.33443828	0.40497290	0.598195 06	0.34725053	0.75739797	0.59610795
b_3/a_0^{-3}	2.2×10^{-9}	6.7×10^{-9}	0.052 923 95	1.3×10^{-8}	5.7×10^{-9}	0.105 297 09

3.2 Three-body energy terms

3.2.1 Three-body dynamical correlation energy

This three-body energy term assumes the following semiempirical form [31]:

$$V_{\rm dc}^{(3)} = -\sum_i \sum_n f_i(\mathbf{R}) C_n^{(i)}(R_i,\theta_i)\chi_n(r_i) r_i^{-n} \tag{17}$$

where r_i, θ_i and R_i are the Jacobi coordinates corresponding to a specific geometry of the triatomic (see Fig. 1 of [25]), and $f_i = \frac{1}{2}\{1-\tanh[\xi(\eta R_i - R_j - R_k)]\}$ is a convenient switching function; corresponding expressions apply to R_j, R_k, f_j, and f_k. Following recent work on HCN [34], we have fixed $\eta = 6$ and $\xi = 1.0\,a_0^{-1}$. Regarding, the damping function $\chi_n(r_i)$, we still adopt [31] Eq. (16) but replace R by the center-of-mass separation for the relevant atom–diatom channel. In addition, the value of ρ has been optimized by a trial- and-error procedure to mimic the asymptotic long-range behavior of the dynamical correlation energy, leading to $\rho = 16.125\,a_0$.

The atom–diatom dispersion coefficents in Eq. (17) assume their usual form

$$C_n^{(i)}(R_i) = \sum_L C_n^L(R) P_L(\cos\theta_i), \tag{18}$$

where $P_L(\cos\theta_i)$ denotes the Lth Legendre polynomial. The expansion in Eq. (18) has been truncated by considering only the coefficients C_6^0, C_6^2, C_8^0, C_8^2, C_8^4, and C_{10}^0; all other coefficients have been assumed to make a negligible contribution, and hence neglected. To estimate the dispersion coefficients we have utilized the generalized Slater–Kirkwood approximation [35] and dipolar polarizabilities calculated in the present work at the MRCI/AVQZ level. As usual, the atom–diatom dispersion coefficients so calculated for a set of internuclear distances have then been fitted to the form

$$C_n^{L,\mathrm{A-BC}}(R) = C_n^{L,\mathrm{AB}} + C_n^{L,\mathrm{AC}} + D_M\left(1+\sum_{i=1}^{3} a_i r^i\right)\exp\left(-\sum_{i=1}^{3} b_i r^i\right) \tag{19}$$

where $C_n^{L,\mathrm{AB}}$, for $L=0$, are the corresponding atom–atom dispersion coefficients (see Table 2; for $L\neq 0$, $C_n^{L,\mathrm{AB}}=0$), and $b_1 = a_1$. The least-squares parameters that result from such fits are collected in Table 3, while their internuclear dependences are displayed in Fig. 3. Note that, for $R=0$, the isotropic component of the dispersion coefficient is fixed at the corresponding value in the A − X pair, where X represents the united atom of BC at the limit of a vanishingly small internuclear separation.

As noted elsewhere [31], Eq. (17) causes an overestimation of the dynamical correlation energy at the atom–diatom dissociation channels. To correct such a behavior, we have multiplied the two-body dynamical correlation energy for the ith pair by $\prod_{j\neq i}(1-f_j)$ (correspondingly for channels j and k). This ensures [31,34] that the only two-body contribution at the ith channel is that of JK.

3.2.2 Three-body extended Hartree–Fock energy

By removing, for a given triatomic geometry, the sum of the one-body and two-body energy terms from the corresponding DMBE–SEC interaction energies in Eq. (1) which were defined with respect to the infinitely separated ground-state atoms, one obtains the total three-body energy. By then subtracting from this the three-body dynamical correlation contribution of Eq. (17), one gets the three-body extended Hartree–Fock energy. This has been modeled via a three-body distributed-polynomial [36] form

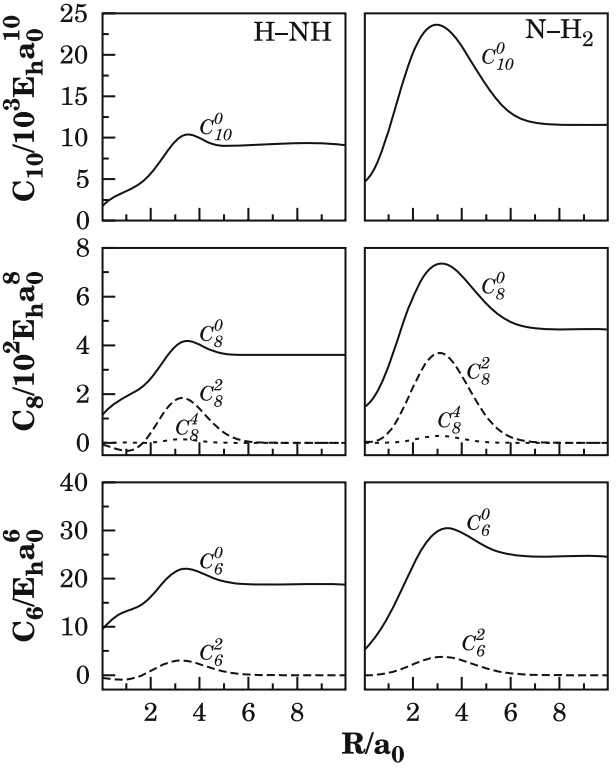

Fig. 3 Dispersion coefficients for the atom–diatom asymptotic channels of NH_2 as a function of the corresponding diatomic internuclear distance

$$V_{\mathrm{EHF}}^{(3)} = \sum_{j=1}^{5} \left\{ P^{(j)}(Q_1, Q_2, Q_3) \times \prod_{i=1}^{3} \left\{ 1 - \tanh\left[\gamma_i^{(j)} \left(R_i - R_i^{(j),\mathrm{ref}} \right) \right] \right\} \right\} \quad (20)$$

where all the polynomials $P^{(j)}(Q_1, Q_2, Q_3)$ are written in terms of symmetry coordinates (for definition of the latter, see, [36]). Note that all polynomials are of sixth order, except the fifth one which is of fourth order. Figure 4 displays the reference geometries that have been used to define the displacement coordinates involved in Eq. (20). To obtain $R_i^{(j),\mathrm{ref}}$, we have first assumed their values to coincide with the bond distances of the associated stationary points. Such a restriction has subsequently been relaxed, with the optimum geometry being obtained via a trial-and-error procedure such as to reduce the root-mean-square-deviation (rmsd) of the final least squares fit. A similar procedure has been employed to set the nonlinear range-determining parameters $\gamma_i^{(j)}$. The complete set amounts to a total of 222 linear coefficients c_i, 15 nonlinear ones $\gamma_i^{(j)}$, and 15 reference geometries $R_i^{(j),\mathrm{ref}}$. A total of $1,532$ points (including those referring to the $N - H_2(^1\Sigma_g^+)$ van der Waals regions, and some interpolated ones) covering an energy range of over $2,400\,\mathrm{kcal\,mol^{-1}}$ above the NH_2 global minimum has been used. Note that special weights have been attributed during the calibration

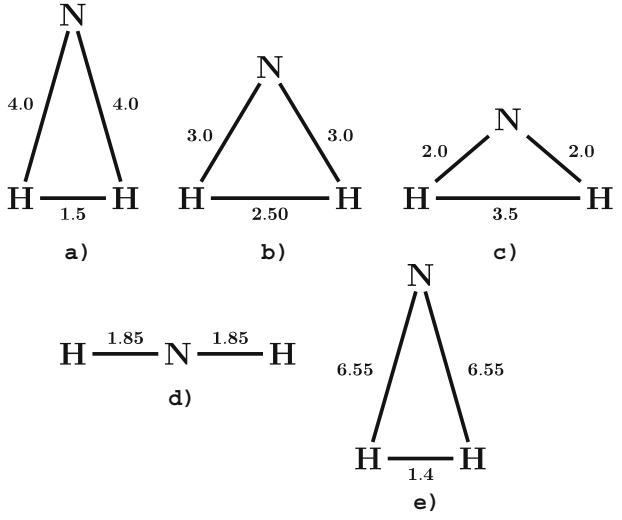

Fig. 4 Reference geometries used to define the three-body extended Hartree-Fock (EHF) part of the potential energy surface (distances in atomic units)

procedure to the points close to stationary points; the complete list of ab initio energies and least-squares weights actually employed for the final fit may be obtained from the authors upon request. Table 4 gathers the values of the least-squares parameters.

The stratified rmsd of the final potential energy surface with respect to all fitted ab initio energies are reported in Table 5. As shown, the final potential energy surface fits the regions up to the linear and C_{2v} barriers ($\sim 130\,\mathrm{kcal\,mol^{-1}}$ above the global minimum) with a rmsd of $< 0.4\,\mathrm{kcal\,mol^{-1}}$ and a maximum deviation of $< 2.8\,\mathrm{kcal\,mol^{-1}}$. Not surprisingly, the major (yet small) deviations occur at highly repulsive regions of the potential energy surface. Despite this, the DMBE form is seen to fit the ab initio data with chemical accuracy, with a stratified rmsd $\ll 1\,\%$ of the energy for the given stratum. Note that only a small percent of the points ($< 16\,\%$, this being for the whole range of energies) have a deviation larger than the calculated rmsd. Thus, although the fit might be improved by adding other polynomials, no attempt was deemed to be justified due to the unavoidable errors at regions close to the crossing seam.

4 Features of the potential energy surface

Table 6 compares the attributes of the stationary points of the DMBE potential energy surface with those of other theoretical potentials for ground state NH_2, especially the most recent work of Ho et al. [7] (see also this reference for further comparisons). As expected, the DMBE surface predicts a lower barrier for the perpendicular insertion of the nitrogen atom into H_2. The predicted geometry and well depth of the global minimum are seen to be basically coincident with those reported by Ho et al. [7] who have based their function on MRCI calculations using an AVTZ basis set (heretofore denoted by MRCI/AVTZ, and correspondingly for other

Table 4 Numerical values of the extended Hartree–Fock (EHF) energy [Eq. (20)]

Coefficients	$P^{(1)}$	$P^{(2)}$	$P^{(3)}$	$P^{(4)}$	$P^{(5)}$
$c_1/a_0{}^0$	0.28972574	−2.23883819	−4.82026636	−10.34547901	0.00336417
$c_2/a_0{}^{-1}$	−0.55810849	1.34798852	−13.32989155	6.82146451	0.00402458
$c_3/a_0{}^{-1}$	0.35597867	2.51479201	5.20391403	−16.51164712	0.00771292
$c_4/a_0{}^{-2}$	0.03011379	0.04660040	−6.98310018	4.19257033	0.01268136
$c_5/a_0{}^{-2}$	0.25264641	0.32033747	−1.76174899	−3.15318437	0.01274666
$c_6/a_0{}^{-2}$	0.07150504	0.07961873	13.14913342	−16.43761499	0.03631929
$c_7/a_0{}^{-2}$	−0.00252553	−0.21360102	2.40680438	−3.61361568	−0.01501876
$c_8/a_0{}^{-3}$	−0.21020530	0.33599947	−2.51660228	2.56964682	0.00517592
$c_9/a_0{}^{-3}$	−0.01034405	−0.02985039	−2.18746772	−3.09554468	0.02417986
$c_{10}/a_0{}^{-3}$	−0.00563727	−0.15730581	−0.58279739	1.17297483	0.00682636
$c_{11}/a_0{}^{-3}$	−0.40826443	0.23927521	3.14929292	−1.27957617	0.02804054
$c_{12}/a_0{}^{-3}$	0.00437155	0.33805178	−1.50882772	4.26944653	−0.02483353
$c_{13}/a_0{}^{-3}$	0.24320295	0.52130976	−0.82580774	−0.49508061	0.02143404
$c_{14}/a_0{}^{-4}$	0.00581370	0.10163321	−0.71370355	0.89781794	−0.00164759
$c_{15}/a_0{}^{-4}$	0.05288872	0.14376423	−2.89543978	1.03355863	−0.00195096
$c_{16}/a_0{}^{-4}$	0.07532079	0.01518369	−0.16687247	0.32623867	0.00319575
$c_{17}/a_0{}^{-4}$	−0.03234647	0.02334543	0.17918664	−1.06417943	0.00349031
$c_{18}/a_0{}^{-4}$	−0.01099316	−0.21441955	3.47245330	−2.63944411	−0.00604896
$c_{19}/a_0{}^{-4}$	0.03642900	0.03273485	1.73645519	−1.18691152	0.00062813
$c_{20}/a_0{}^{-4}$	0.15570612	−0.05901273	2.18616814	−4.71082073	0.00668133
$c_{21}/a_0{}^{-4}$	−0.03994482	−0.02320849	−0.18076633	1.00046730	0.00318550
$c_{22}/a_0{}^{-4}$	−0.05956185	0.07340589	0.14178975	−0.67036214	−0.00255943
$c_{23}/a_0{}^{-5}$	−0.00621797	−0.00084108	−0.06377893	0.14299508	
$c_{24}/a_0{}^{-5}$	−0.02764205	−0.05366966	0.53031223	−0.99916190	
$c_{25}/a_0{}^{-5}$	0.01514678	−0.02402850	0.43331974	−0.82278451	
$c_{26}/a_0{}^{-5}$	−0.02854379	−0.01843950	−0.36266437	0.22691603	
$c_{27}/a_0{}^{-5}$	−0.01063750	−0.00336688	−0.16888422	0.40056270	
$c_{28}/a_0{}^{-5}$	−0.02862361	0.02767599	−0.27565869	0.75973486	
$c_{29}/a_0{}^{-5}$	0.02458300	−0.00764734	−0.33960193	0.95557878	
$c_{30}/a_0{}^{-5}$	−0.02140507	0.08481649	−0.99355561	1.23475350	
$c_{31}/a_0{}^{-5}$	−0.05777760	−0.01127916	0.37535466	−0.18269793	
$c_{32}/a_0{}^{-5}$	−0.01665148	0.05385674	−0.57480428	0.97068822	
$c_{33}/a_0{}^{-5}$	0.02122847	0.01730448	−0.33531560	0.49320770	
$c_{34}/a_0{}^{-5}$	0.01914194	−0.01763677	0.06028977	−0.22657901	
$c_{35}/a_0{}^{-6}$	0.00247218	0.00528895	−0.02671849	0.01997170	
$c_{36}/a_0{}^{-6}$	−0.01211048	0.00385499	−0.14913457	0.03988751	
$c_{37}/a_0{}^{-6}$	−0.00711497	−0.00795683	−0.18350113	0.19528166	
$c_{38}/a_0{}^{-6}$	−0.01872577	−0.00071293	0.16239653	−0.07885454	
$c_{39}/a_0{}^{-6}$	−0.01205357	−0.00401599	0.12562857	−0.09168383	
$c_{40}/a_0{}^{-6}$	0.00413216	−0.00077721	−0.02558218	0.02345618	
$c_{41}/a_0{}^{-6}$	−0.00414042	−0.00042295	−0.01396550	0.02710977	
$c_{42}/a_0{}^{-6}$	0.00126063	−0.01642519	0.17919501	−0.03676125	
$c_{43}/a_0{}^{-6}$	0.01332372	−0.00906645	0.21487615	−0.00597842	
$c_{44}/a_0{}^{-6}$	−0.03787771	0.00117807	0.31174108	−0.28878921	
$c_{45}/a_0{}^{-6}$	−0.02600113	0.00820752	−0.19069192	0.07088748	
$c_{46}/a_0{}^{-6}$	0.01181454	0.00821036	0.15454689	−0.24948561	
$c_{47}/a_0{}^{-6}$	0.00951985	0.01190600	0.15238190	−0.23974016	
$c_{48}/a_0{}^{-6}$	0.01278203	0.00159730	−0.06594640	0.01599530	
$c_{49}/a_0{}^{-6}$	−0.00486393	0.00644670	−0.08568753	0.10016699	
$c_{50}/a_0{}^{-6}$	−0.00142419	−0.00027149	0.01609771	−0.02005957	

Table 4 (Contd.)

Coefficients	$P^{(1)}$	$P^{(2)}$	$P^{(3)}$	$P^{(4)}$	$P^{(5)}$
$\gamma_1^{(j)}/a_0{}^{-1}$	1.45	0.40	0.35	0.75	3.95
$\gamma_2^{(j)}/a_0{}^{-1}$	0.50	0.80	0.85	0.75	0.65
$\gamma_3^{(j)}/a_0{}^{-1}$	0.50	0.80	0.85	0.75	0.65
$R_1^{(j),\mathrm{ref}}/a_0$	1.50	2.50	3.50	3.70	1.40
$R_2^{(j),\mathrm{ref}}/a_0$	4.00	3.00	2.00	1.85	6.55
$R_3^{(j),\mathrm{ref}}/a_0$	4.00	3.00	2.00	1.85	6.55

Table 5 Stratified maximum and root-mean-square deviations (in kcal mol^{-1}) of double many-body expansion (DMBE) potential energy surface

Energy	N[a)]	max. dev.[b)]	rmsd	$N_{>\mathrm{rmsd}}$[c)]
10	127	0.187	0.031	13
20	141	0.205	0.045	17
30	159	2.160	0.189	8
40	184	2.160	0.251	15
50	197	2.160	0.255	20
60	218	2.160	0.283	30
70	236	2.160	0.289	37
80	259	2.160	0.296	45
90	292	2.160	0.311	55
100	404	2.160	0.286	71
120	600	2.515	0.341	88
140	922	2.855	0.359	143
160	1,197	2.855	0.378	193
180	1,372	3.304	0.409	222
200	1,421	3.806	0.428	224
250	1,442	3.806	0.442	227
500	1,475	3.806	0.457	238
1000	1,493	3.806	0.474	237
2000	1,497	3.806	0.474	239
2400	1,498	3.806	0.474	240

[a)] Number of calculated multi-reference configuration interaction/ aug-cc-pVQZ (MRCI/AVQZ) and aug-cc-p V5Z (AV5Z) points up to the indicated energy range

[b)] Maximum deviation up to the indicated energy range

[c)] Number of calculated MRCI/AVQZ and AV5Z points with an energy deviation larger than the root-mean-square deviation (rmsd)

basis sets). Note that the scaling of the dynamical correlation leads to a MRCI/AVQZ well depth for $NH_2(\tilde{X}\,^2B_1)$ of 126.4 kcal mol^{-1} which is identical to the one obtained from the MRCI/AVTZ calculations after correcting for the triple and quadruple excitations using the Davidson correction [11] (except where mentioned otherwise, we will keep the notation MRCI/AVTZ to denote the corrected calculations at this level). Note further that the uncorrected MRCI/AVTZ calculations [11] lead to a well depth of 125.5 kcal mol^{-1}, which compares with the value of 125.9 kcal mol^{-1} obtained in the present work at the corresponding MRCI/AVQZ level. Thus, for the AVTZ calculations, the Davidson correction leads to a further increase of 0.4 kcal mol^{-1} in the well depth of $NH_2(\tilde{X}\,^2B_1)$ when compared with the MRCI/AVQZ results from the present work after correction by the DMBE–SEC method. Table 6 also shows that the harmonic frequencies are very similar for the MRCI/AVTZ and DMBE-SEC surfaces, with the differences being smaller than about 50 cm^{-1}. The same observation extends to the DMBE surface. We emphasize that a dense grid of points has been calculated in the vicinity of the global minimum, with the rmsd of the DMBE least-squares fit to such points being $\sim$ 0.3 cm^{-1} ($\sim$ 0.08 cm^{-1} for the direct fit of a cubic polynomial in valence coordinates to the DMBE–SEC data).

For the C_{2v} barrier, the DMBE potential energy surface predicts a barrier height which is 0.36 kcal mol^{-1} higher than that predicted by the Ho et al. [7] form (0.23 kcal mol^{-1} higher than their previous ab initio estimate [11]) but 0.15 kcal mol^{-1} below the MRCI calculations reported by Takayanagi et al. [37] using a somewhat less flexible

Table 6 Stationary points at the valence region of $NH_2(1\,^2A'')$ potential energy surface

Feature	Property	Ab initio[a]	Ab initio[b]	RKHS[b,c]	DMBE-SEC[d]	DMBE[c,d]
Global minimun	R_1/a_0		3.04	3.04	3.0288	3.0291
	R_2/a_0		1.9445	1.94	1.9406	1.9405
	r_1^e/a_0		1.21	1.20	1.2135	1.2131
	∠HNH[f]		102.7°	102.7°	102.6°	102.6°
	V/E_h				−0.2858	−0.2858
	ΔV^g		−126.4	−126.4	−126.4	−126.4
	$\omega_1(N-H)_{sym}/cm^{-1}$		3,340	3,350	3,377	3,383
	$\omega_2(N-H)_{asym}/cm^{-1}$		3,435	3,436	3,443	3,457
	$\omega_3(bend)/cm^{-1}$		1,542	1,559	1,523	1,541
C_{2v} barrier	R_1/a_0	1.42	1.42	1.42	1.4203	1.4198
$N(^2D)-H_2$	R_2/a_0	3.96	4.05	4.05	3.9561	3.9349
	r_1/a_0	3.90	3.99	3.99	3.8918	3.8703
	∠HNH	20.7°	20.2°	20.2°	20.7°	20.8°
	V/E_h				−0.0809	−0.0809
	ΔV^g	2.31	1.8	1.8	2.16	2.16
	$\omega_1(H-H)(cm^{-1})$		4,239	4,240	4,223	4,209
	$\omega_2(N\cdots H_2)(cm^{-1})$		501*i*	499*i*	547*i*	499*i*
	$\omega_3(H_2\ rot.)(cm^{-1})$		324	325	385	282
$C_{\infty v}$ barrier	R_1/a_0	1.52	1.539	1.54		1.5121
N − H − H	R_2/a_0	2.94	2.913	2.93		2.9010
	r_1/a_0	3.70	3.68	3.70		3.6570
	V/E_h					−0.0763
	ΔV^g	4.61	4.8	4.8		5.1
	$\omega_1(H-H)(cm^{-1})$		3,031	2,616		2,671
	$\omega_2(N-H)(cm^{-1})$		1,031*i*	1,032*i*		1,455*i*
	$\omega_3(bend)(cm^{-1})$		818*i*	764*i*		844*i*

a) Ref. [37].
b) Ref. [7].
c) Fit.
d) This work.
e) The experimental value reported in [11] is 1.21 a_0.
f) The experimental value reported in [11] is 103.0°
g) Relative to the $N(^2D)+H_2$ asymptote (in kcal mol^{-1}). At this limit, the full valence complete active space (FVCAS) and MRCI/aug-cc-pVQZ energies are −55.45066862 E_h and −55.60375691 E_h, respectively

cc-pVTZ basis set. Note that those potential energy surfaces [7,11,37] employ ab initio diatomic curves calculated at the corresponding level of ab initio theory, whereas in our case they have been corrected by scaling the dynamical correlation such that the full curve mimics the best available estimate for the well depth (see Sect. 2). Recall now that the three-body scaling factor used in the DMBE–SEC method is obtained as the average of the two-body ones. Thus, the attributes of the triatomic potential are true predictions of the method. For example, the calculated bond length and dissociation energy for H_2 (including the one-body term referring to the energy difference between the ^4S and ^2D electronic states of atomic nitrogen) at the MRCI/AVTZ level are $R_e = 1.404\,a_0$ and $D_e = -0.082762\,E_h$ while the corresponding attributes of the EHFACE2U (or SEC) curve are $R_e = 1.401\,a_0$ and $D_e = -0.084336\,E_h$. As shown in Fig. 5, the H_2 asymptote in the DMBE potential energy surface lies therefore 0.987 kcal mol^{-1} below the MRCI/AVTZ curve obtained by interpolation using the RKHS method [7]. Similarly, a fit to the dense grid of unscaled MRCI/AVQZ points close to the C_{2v} saddle point calculated in the present work leads to a barrier height relative to the unscaled MRCI/AVQZ curve for H_2 of 2.19 kcal mol^{-1}, i.e., the scaling of the dynamical correlation is predicted to yield a stabilization of only 0.03 kcal mol^{-1} relatively to the unscaled calculations. Assuming that the Davidson correction would lead to an extra lowering similar to the value encountered for the equilibrium geometry, one would predict a barrier height for the C_{2v} insertion of $N(^2D)$ into H_2 of $2.19 - 0.4 - 0.03 = 1.76$ kcal mol^{-1}, in surprisingly good agreement with the value of 1.8 kcal mol^{-1} reported for the MRCI/AVTZ calculations [7,11]. Instead, if we use their estimated [7,11] AVTZ Davidson correction (0.36 kcal mol^{-1}) at the C_{2v} saddle point one gets $2.19 - 0.39 = 1.8$ kcal mol^{-1}, which yields an AVQZ barrier height identical to the AVTZ one. This by no means implies that the inclusion of the Davidson correction leads to a more reliable barrier height than the DMBE–SEC method. In fact, this method has by construction the advantage of mimicking the exact atom+diatomic asymptote at the equilibrium geometry of the diatomic molecule. Thus, further ab initio work and possibly dynamical calculations are necessary to ascertain which of the above estimates

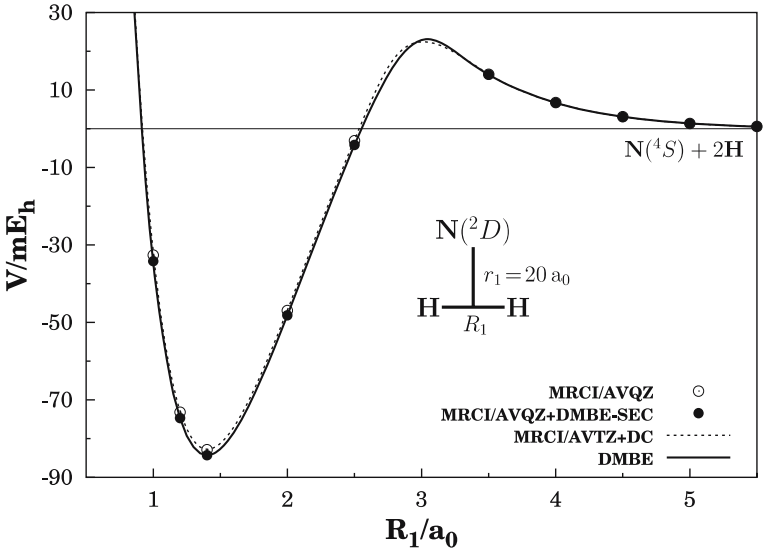

Fig. 5 A comparison of the H_2 potential energy curves including the one-body term referring to the $N(^2D) - N(^4S)$ excitation energy. The *dashed line* shows the MRCI/AVTZ curve obtained by interpolation using the reproducing Kernel-Hilbert space (RKHS) method [7], while the curve associated to the present DMBE potential energy surface is indicated by the *solid line*. Also shown are the MRCI/AVQZ (*open dots*) and MRCI/AVQZ+DMBE-SEC (*solid dots*) energies calculated at $r = 20\,a_0$. The reference energy refers to $N(^4S) + H + H$

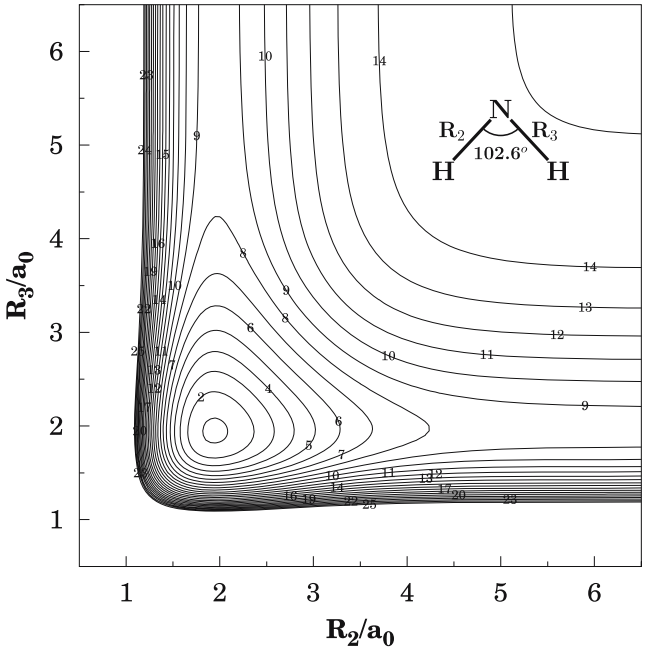

Fig. 6 Contour plot for bond stretching in H − N − H, keeping the included angle fixed at 102.5°. Contours are equally spaced by 0.02 E_h, starting at −0.282 E_h

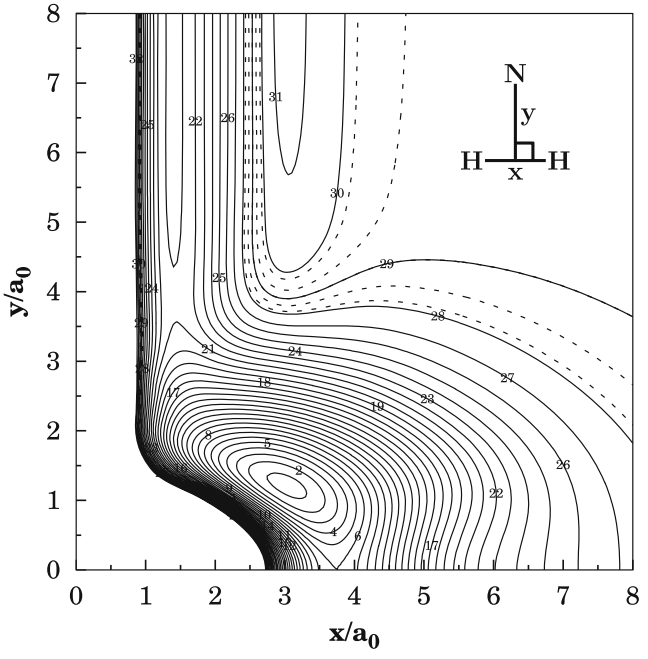

Fig. 7 Contour plot for the C_{2v} insertion of the N atom into H_2. Contours are equally spaced by 0.01 E_h, starting at −0.282 E_h. Shown in *dashed* are contours equally spaced by 0.004 E_h, starting at −0.01 E_h.

(1.8 vs. 2.1 kcal mol^{-1}) is the most realistic one. Finally, Table 6 shows that there is a fairly good agreement between the DMBE and RKHS [7] potential energy surfaces as far the calculated vibrational frequencies are concerned, with the largest absolute deviations not generally exceeding 60 cm^{-1}. Such deviations remain small when comparing the results obtained by fitting a local polynomial with those obtained from the DMBE potential energy surface, which corroborates the high quality of the present global fit.

The linear barrier has only been modeled via the final DMBE fit, and hence its attributes may not have been so definitely characterized. It is seen that the barrier height slightly overestimates previous theoretical values. Perhaps not surprisingly, somewhat larger differences are also observed

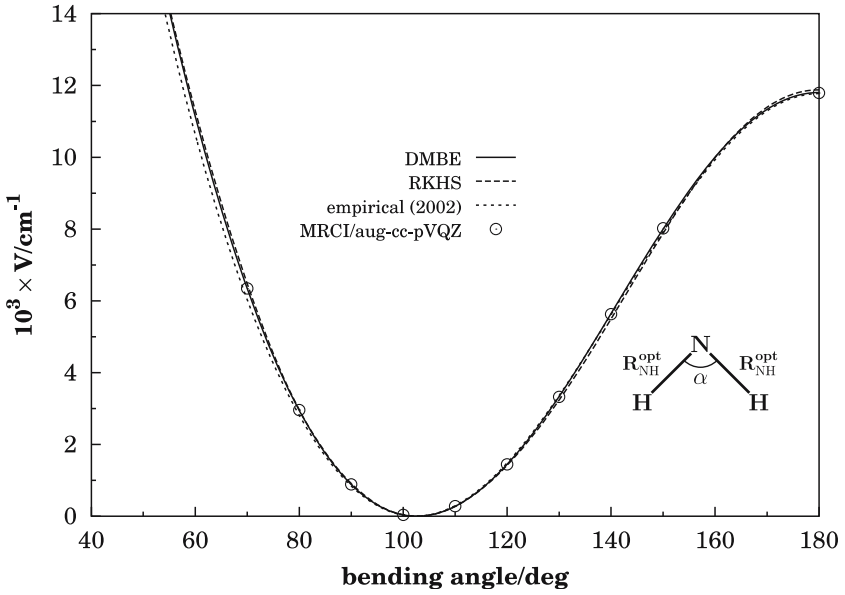

Fig. 8 Optimized C_{2v} bending curve: *dashed line*, RKHS [7], *dotted line*, empirical [14]; *continuous line*, DMBE (this work)

for the corresponding harmonic frequencies. Despite this, we may judge our results as providing an accurate representation of the true potential energy surface at the chosen level of theory.

Figures 6, 7, 8, 9, 10, and 11 illustrate the major topographical features of the $NH_2(\tilde{X}^2B_1)$ DMBE potential energy surface. Clearly, it has a smooth and correct behavior over the whole configuration space. Also visible are its major stationary points: C_{2v} and linear barriers, and the global minimum. Moreover, we observe from Fig. 7 the $D_{\infty h}$ saddle point associated to the linear $^2\Pi$ structure where the $\tilde{X}$ and $\tilde{A}$ Renner–Teller states of NH_2 become degenerate. This stationary point has been properly characterized, and found to lie $11,802\,\mathrm{cm}^{-1}$ above the minimum of the NH_2 potential energy surface at a $D_{\infty h}$ geometry with characteristic bond length of $R_2 = R_3 = 1.8695\,a_0$ and frequencies of $\omega_1(\mathrm{N-H})_{\mathrm{symm}} = 3,676\,\mathrm{cm}^{-1}$, $\omega_2(\mathrm{N-H})_{\mathrm{asym}} = 6,979\,\mathrm{cm}^{-1}$, and $\omega_3(\mathrm{bend}) = 1,544\,\mathrm{cm}^{-1}$. Such a point corresponds to the maximum at 180° in the optimized bending plot of Fig. 8, and corresponds in the RKHS function to a bending barrier of $11,879\,\mathrm{cm}^{-1}$. A notable feature from this plot is the fairly good agreement between our optimized bending curve and the one that we have obtained from the RKHS [7] potential energy surface, which exceeds the most recent empirical estimate [14] for the bending barrier height by $105\,\mathrm{cm}^{-1}$. Interestingly, such a barrier for linearization is predicted by the DMBE potential energy surface to be only $28\,\mathrm{cm}^{-1}$ larger than the empirical result obtained from the effective one-dimensional bending potential model of Duxbury and Alijah [14]. Indeed, the agreement with the latter is excellent over the whole range of angles shown in Fig. 8, particularly for values larger than equilibrium where the optimized DMBE curve is almost indistinguishable from the empirical curve [14] within the scale of the figure. This is

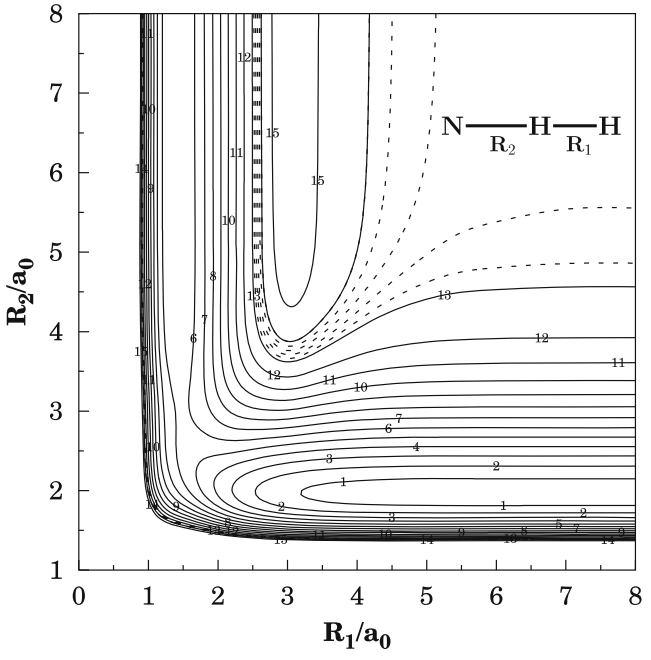

Fig. 9 Contour plot for bond stretching in linear N − H − H configurations. Contours are equally spaced by 0.01 E_h, starting at −0.125 E_h. Shown in *dash* are contours equally spaced by 0.002 E_h, starting at −0.003 E_h

a remarkable result since our fitted ab initio MRCI data points correspond to energies computed for an optimized characteristic bond length at each value of the valence angle (∠HNH). We should also emphasize that the ab initio points of the dense grid encompassing the $^2\Pi$ structure have been highly weighted in the least-squares fitting procedure such as to warrant an accurate description of the topographical features

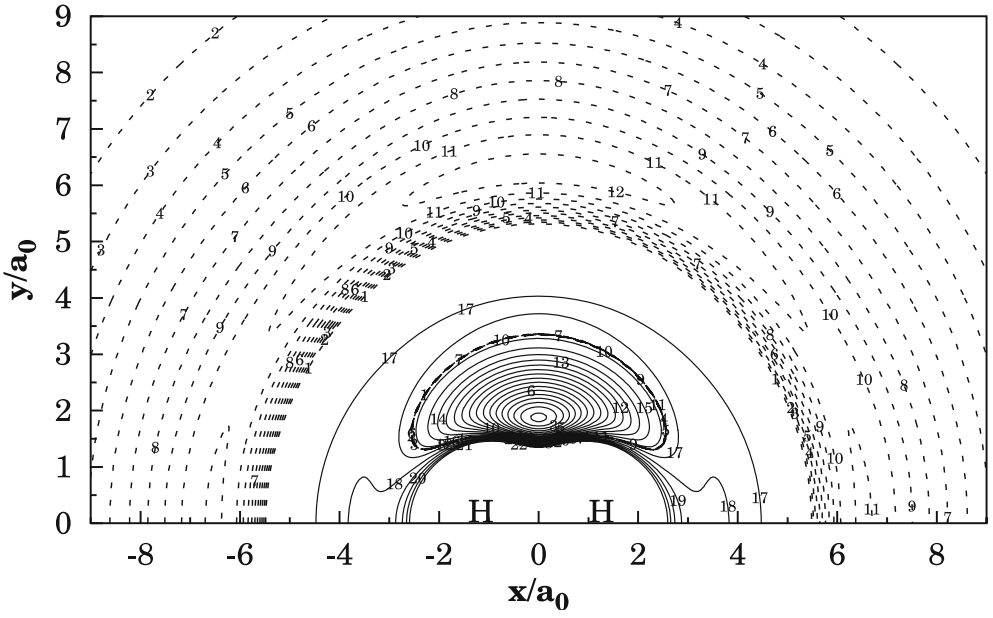

Fig. 10 Contour plot for a N atom moving around a H_2 molecule fixed at the equilibrium geometry $R_1 = 1.401\ a_0$ and lying along the X-axis with the center of the bond fixed at the origin. Contours are equally spaced by $0.005\ E_h$, starting at $-0.161\ E_h$. Shown in *dash* are contours equally spaced by $-0.000035\ E_h$, starting at $-0.084336\ E_h$

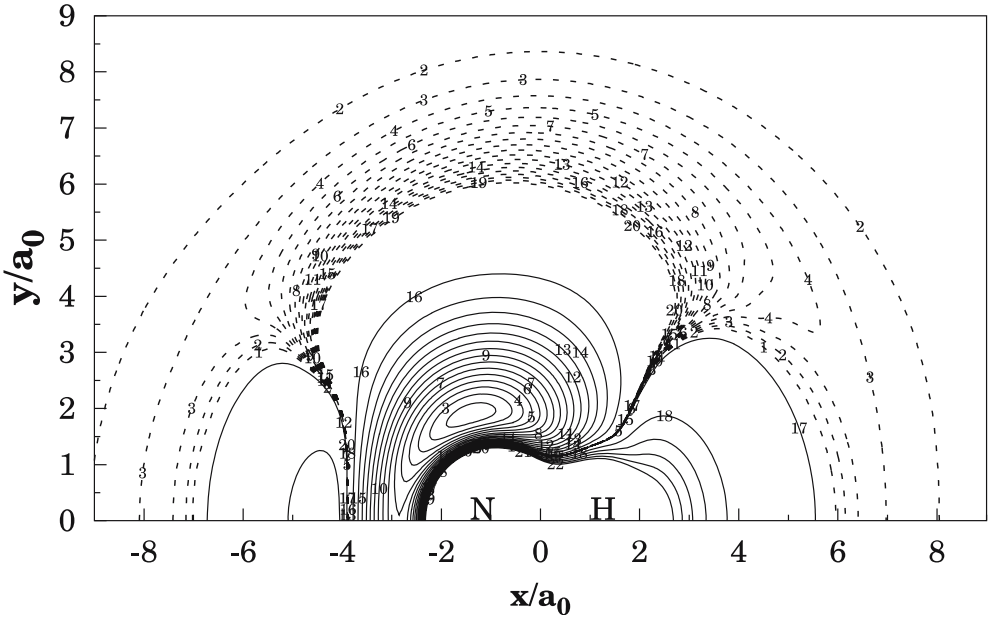

Fig. 11 Contour plot for a H atom moving around a NH diatomic fixed at the equilibrium geometry, $R_{NH} = 1.965\ a_0$, which lies along the X-axis with the center of the bond fixed at the origin. Contours are equally spaced by $0.01\ E_h$, starting at $-0.29\ E_h$. Shown in *dash* are contours equally spaced by $-0.00005\ E_h$, starting at $-0.130208\ E_h$

of potential energy surface at those regions of configuration space. Thus, we corroborate the recent trend to diminish the barrier for linearization when comparing with earlier theoretical [12] and empirical [38] estimates.

Figures 10 and 11 illustrate also the long range part of the potential energy surface which was fitted such as to provide a reliable description of the van der Waals minimum for the $N - H_2$ interaction: the rmsd of all fitted points (with $N - H_2$ distances larger than $5a_0$) in the energy range between the van der Waals minimum and the dissociation limit, in a total of 44 points, is $6.4\ cm^{-1}$. Note that it shows a flat van der Waals valley, with two minima: one at a C_{2v} geometry and the other at a $C_{\infty v}$ one. Of these, the deepest minimum refers to the T-shaped structure, although its well depth is only $0.032\ kcal\ mol^{-1}$ ($11.2\ cm^{-1}$) larger than that of the collinear one; see Table 7 for other attributes. It should be pointed

Table 7 Attributes of $N(^2D) - H_2$ van der Waals minima

Feature	RKHS[a]	DMBE[b]		
		C_{2v} min.[c]	$C_{\infty v}$ min.[c]	C_s s.p.[d]
R_{H-H}/a_0	1.405	1.3995	1.3994	1.3990
R_{N-H}/a_0	5.5571	6.2996	5.8191	5.7847
∠NHH	180°	90°	180°	153°
ΔV (kcal mol^{-1})	−0.2761	−0.2510[e]	−0.2228[e]	−0.2197[e]
ω_1^f(intra)(cm^{-1})	4,392	4,428	4,394	4,405
ω_2^g(inter)(cm^{-1})	231	79	63	73
ω_3^h(bend)(cm^{-1})	81	57	58	64i

[a]Ref. [7]
[b]This work
[c]van der Waals minimum
[d]Saddle point connecting the two van der Waals minima
[e]Relative to the $N(^2D) + H_2$ asymptote which is −55.45143412 E_h and −55.60727004 E_h at the FVCAS and MRCI/aug-cc-pV5Z levels, respectively
[f]Associated to the intramolecular diatomic stretching frequency
[g]Associated to the intermolecular atom-diatom stretching frequency
[h]Associated to the bending (nearly free-rotor) motion

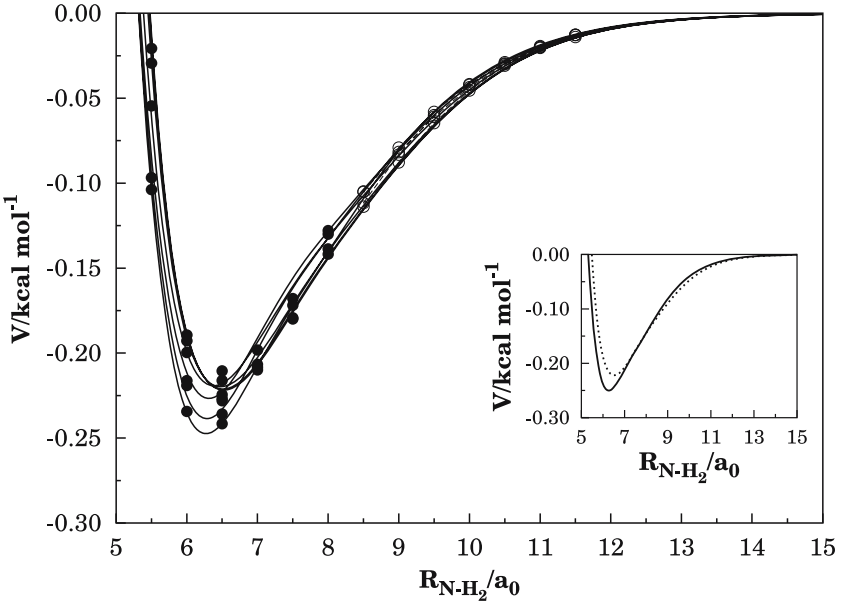

Fig. 12 Cut of DMBE potential energy surface along the atom–diatom radial coordinate for a fixed diatomic bond distance of $R_1 = 1.401\ a_0$. The *solid points* indicate the actually calculated MRCI/AV5Z energies, while the *open circles* have been estimated by using an extended-Rydberg form (see the text). Shown in the inset are the curves for 0° and 90°, which cross each other at about $r_1 = 8.5\ a_0$.

Table 8 Attributes of leading terms in Legendre expansion of $N(^2D) - H_2$ van der Waals potentials

Feature	RKHS[a]	DMBE[b]
Spherically averaged potential, V_0		
R_m^c(a$_0$)	6.30	6.31
ϵ^d(kcal mol^{-1})	0.160	0.236
Leading anisotropic term, V_2		
R_m^c(a$_0$)	6.10	9.59
ϵ^d(kcal mol^{-1})	0.052	0.005

[a]Ref. [7]
[b]This work
[c]Geometry of van der Waals minimum
[d]Well depth of van der Waals minimum

out that the van der Waals energies have been carefully fitted by attributing large weights to the corresponding points. Note that these energies correspond for $N \cdots H_2$ to AV5Z calculations, which are computationally demanding and hence have been carried out only for a small number of geometries. To avoid oscillations in the final DMBE form, a number of other points have been obtained by interpolation using reliable local procedures. For example, along the atom–diatom coordinate (R), we have used an extended-Rydberg form $V = -D(1 + \sum_{i=1}^{N} a_i s^i) \exp(-a_1 s)$ to interpolate between the calculated points; $s = R - R_m$ is the displacement coordinate from the minimum associated to the chosen angle, and

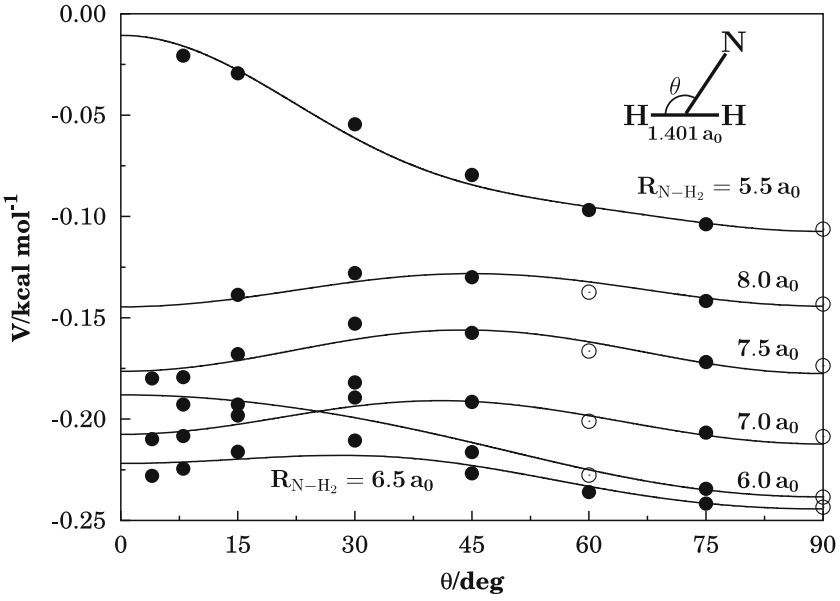

Fig. 13 Cut of DMBE potential energy surface along the Jacobi angle for a fixed diatomic bond distance of $R_1 = 1.401$ a$_0$. Symbols as in Fig. 12.

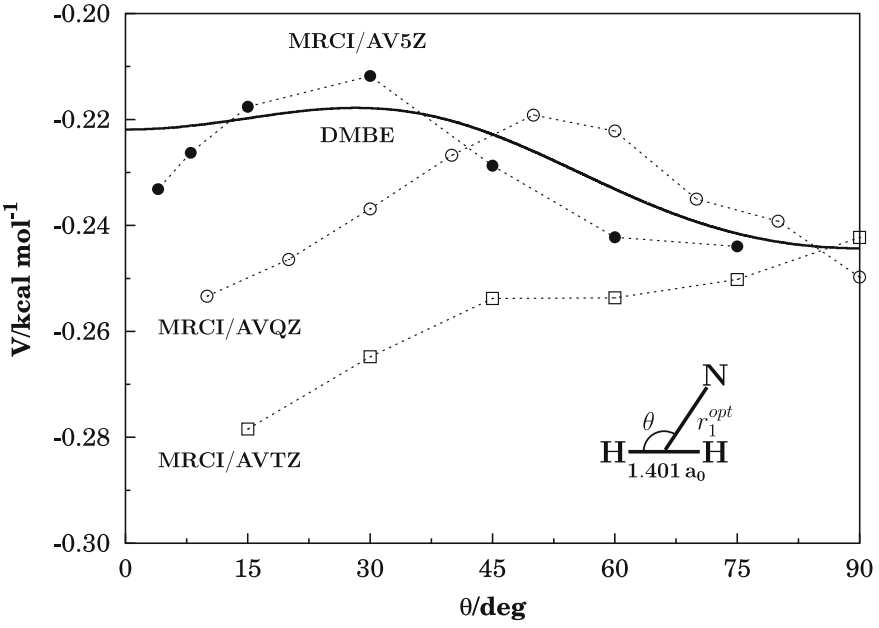

Fig. 14 A comparison of the ab initio minimum energy paths for isomerization between the collinear and T-shaped van der Waals structures. Also indicated is the corresponding path for the DMBE potential energy surface. For each Jacobi angle, the ab initio results have been obtained via a quadratic interpolation. The diatomic bond distance has been fixed at $R_1 = 1.401$ a$_0$

D and a_i are least-squares parameters. Such a procedure has also been employed to generate points at the intermediate distances between the last calculated point and the asymptote where the dynamical correlation energy by far dominates. Instead, to generate a few points at C_{2v} geometries where their convergence proved unsatisfactory, we have chosen a parabolic angular dependence centered at 90°. As shown in the one-dimensional plots of Figs. 12 and 13, the final DMBE form reproduces quite satisfactorily all fitted data. It should be emphasized that the topography of the AV5Z potential energy surface at the N $\cdots$ H_2 van der Waals region differs drastically from the one calculated at the MRCI/AVTZ level, while the MRCI/AVQZ one is intermediate and confirms the tendency to the AV5Z results. This is illustrated in Fig. 14, which shows the MRCI minimum energy paths for the above three correlated consistent basis sets as a function of the Jacobi angle (the points are approximate, and have been obtained by interpolation of the three calculated energies closest to the minimum for a given Jacobi angle by using a quadratic form). Also indicated for comparison is the curve associated

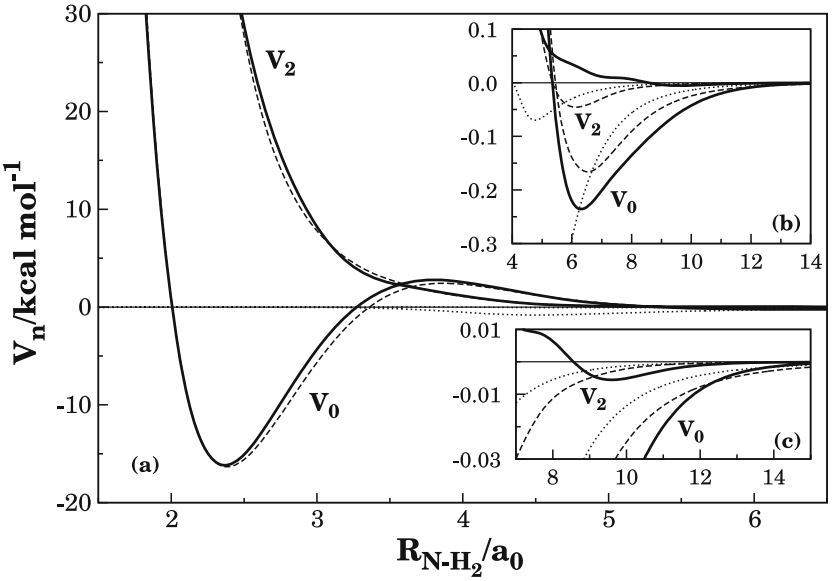

Fig. 15 Isotropic (V_0) and leading anisotropic (V_2) components of the $N - H_2$ interaction potential, with the diatomic molecule fixed at the equilibrium geometry. *continuous line*, DMBE; *dashed line*, RKHS; *dotted line*, three-body dynamical correlation term (leading to asymptotic atom–diatom dispersion interaction at large distances) in Eq. (17). The axes in all panels have the same units. Note that in all *panels* the *dotted line* lying closest to the $r_1 = R_{N-H_2}$ axis at the reference energy refers to V_2

to the DMBE potential energy surface. Clearly, the agreement with the MRCI/AV5Z results is rather satisfactory, especially recalling the discrepancy amongst the ab initio results themselves. Of course, an improvement could be obtained either by increasing the order of the polynomial centered at the T-shaped van der Waals minimum or adding an extra polynomial centered at the linear van der Waals structure. For the reasons given in Sect. 3 and given the coarse grid of calculated MRCI/AV5Z points, such an approach did not seem justified. In turn, the $H \cdots NH$ channel is purely attractive, and hence no such calculations have been judged to be necessary there.

The isotropic and leading anisotropic potentials are two important quantities for the study of $N - H_2$ scattering processes [39], being shown in panels (a)–(c) of Fig. 15 and Table 8. Specifically, the isotropic average potential V_0 determines how close on average the atom and molecule can approach each other, while the magnitude of V_2 indicates whether or not the molecule prefers to orient its axis along the direction of the incoming atom: a negative value favors the collinear approach while a positive value favors the approach through an isosceles triangular geometry. The barrier in V_0 located near 3.5 a_0 (see panel (a) of Fig. 15) corresponds to the C_{2v} transition state, as corroborated by the positive value of V_2 at such a distance. In turn, the negative sign of V_2 at distances larger than 8.5 a_0, indicates that the van der Waals interaction energy is larger for such collinear geometries (see panel (b) of Fig. 15) as one would expect from the larger polarizability of the hydrogen molecule along the internuclear axis. Note, however, that the anisotropy is positive at the region of the van der Waals minimum in the isotropic potential (V_0). This is due to the deepest well associated to the T-shaped van der Waals structure. This contrasts with the RKHS surface, which predicts the van der Waals minimum to occur at a collinear geometry. Recall that the MRCI calculations carried out using AVTZ, AVQZ, and AV5Z basis sets corroborate the tendency to a shallow van der Waals valley (see Fig. 13), with minima being located both at T-shaped and collinear structures. The small bump in V_2 between 6.5 and 7.5 a_0 may be attributed to the fact that the T-shaped minimum occurs at a slightly smaller atom–diatom bond distance than the collinear van der Waals structure. Since the $N(^2D) + H_2$ reaction has been shown to display a preference to occur via an insertion mechanism, it is possible that this subtle detail may have practical implications for the scattering especially at low collision energies. We further observe that the spherically averaged component of the RKHS [7] surface has a slightly shallower van der Waals minimum in comparison with the DMBE one but is somewhat more attractive at large distances (see Table 8 for the numerical attributes of V_0 and V_2). Moreover, the DMBE potential energy surface has a significantly smaller anisotropy (the well depth of V_2 is only 1.6 cm^{-1}) than the RKHS [7] surface in accordance with the trends predicted from the MRCI calculations; see the insert of Figs. 12 and 14. Finally, we emphasize (see panel (c) of Fig. 15) that the current potential energy surface reproduces the assumed long-range interactions described in Sect. 3.2.1 both at the $N(^2D) + H_2$ and $H \cdots NH$ asymptotes, a major general asset of DMBE theory.

5 Concluding remarks

We have suggested an improved switching function formalism that allows an accurate description of the ground state potential energy surface of NH_2 by a single-sheeted DMBE form. This has been calibrated from newly calculated MRCI

energies distributed over all geometries of chemical relevance. Given the high level of the calculated ab initio energies, the resulting DMBE potential energy surface is possibly the most accurate function reported thus far for the title system, although it lies close to that obtained via a RKHS interpolation [7]. Clearly, a more definite assessment of the accuracy of the DMBE potential energy surface[1] cannot be made prior to use in dynamics calculations. Its simplicity and quality suggest though that it should be recommendable for both reactive and non-reactive studies of $N(^2D) + H_2$ collisions.

Acknowledgment

This work has the support of Fundação para a Ciência e Tecnologia, Portugal, under programmes POCTI and FEDER. The partial support of the European Community's Human Potential Programme under contract HPRN-CT-2002-00170 is also appreciated.

References

1. Suzuki T, Shihira Y, Sato T, Umemoto H, Tsunashima S (1993) J Chem Soc Faraday Trans 89:995
2. Kobayashi H, Takayanagi T, Yokoyama K, Sato T, Tsunashima S (1995) J Chem Soc Faraday Trans 91:3771
3. Dodd JA, Lipson SJ, Flanagan DJ, Blumberg WAM, Pearson JC, Green BD (1991) J Chem Phys 94:4301
4. Umemoto H, Matsumoto K (1996) J Chem Phys 104:9640
5. Umemoto H, Asai T, Kimura Y (1997) J Chem Phys 106:4985
6. Alagia M, Balucani N, Cartechini L, Cachavecchia P, Volpi GG, Pederson LA, Schatz GC, Lendvay G, Harding LB, Hollebeek T, Ho T-S, Rabitz H (1999) J Chem Phys 110:8857
7. Ho T-S, Rabitz H, Aoiz FJ, Bañares L, Vázquez SA, Harding LB (2003) J Chem Phys 119:3063
8. Aronszajn N (1950) Trans Am Math Soc 68:337
9. de Boor C, Lynch R (1966) J Math Mech 15:953
10. Davis PJ (1975) Interpolation and approximation, Dover, New York
11. Pederson LA, Schatz GC, Ho T, Hollebeek T, Rabitz H, Harding LB (1999) J Chem Phys 110:9091
12. Buenker RJ, Perić M, Peyerimhoff SD, Marian R (1981) Mol Phys 43:987
13. Gabriel W, Chambaud G, Rosmus P, Carter S, Handy N, (1994) Mol Phys 6:1445
14. Duxbury G, Alijah A (2002) J Mol Spectrosc 211:31
15. Varandas AJC (1988) Adv Chem Phys 74:255
16. Varandas AJC (2000) Lecture notes in chemistry. In: Laganá A, Riganelli A (eds) Vol. 75. Springer, Berlin Heidelberg New York p 33
17. Varandas AJC (2004) Conical intersections: electronic structure, dynamics and spectroscopy. In: Yarkony D, Köppel H, Domcke W (eds) Chap. 5. World Scientific Publishing, Singapore p 205
18. Murrell JN, Carter S (1984) J Phys Chem 88:4887
19. Dunning TH (1989) J Chem Phys 90:1007
20. Kendall R, Dunning T Jr, Harrison R (1992) J Chem Phys 96:6769
21. Varandas AJC (1989) J Chem Phys 90:4379
22. Werner H-J, Knowles PJ (1988) J Chem Phys 89:5803
23. Knowles PJ, Werner H-J (1985) Chem Phys Lett 115:259
24. Werner H-J, Knowles PJ (1998) MOLPRO is a package of ab initio programs written by Werner H-J, Knowles PJ, with contributions from Almlöf J, Amos RD, Deegan MJO, Elbert ST, Hampel C, Meyer W, Peterson KA, Pitzer R, Stone AJ, Taylor PR, Lindh R
25. Varandas AJC (1992) Chem Phys Lett 194:333
26. Anderson WR (1989) J Phys Chem 93:530
27. Boys F, Bernardi F (1970) Mol Phys 19:553
28. Varandas AJC, Silva JD (1992) J Chem Soc Faraday Trans 88:941
29. Varandas AJC (1985) J Mol Struct Theochem 120:401
30. Le Roy RJ (1973) Spec Period Rep Chem Soc Mol Spectrosc 1:113
31. Varandas AJC (1996) J Chem Phys 105:3524
32. Varandas AJC, Rodrigues SPJ (1997) J Chem Phys 106:9647
33. Stallcop JR, Bauschlicher CW, Partridge H, Langhoff SR, Levin E (1992) J Chem Phys 97:5579
34. Varandas AJC, Rodrigues SPJ (2006) J Phys Chem A 110:485
35. Matías MA, Varandas AJC (1990) Mol Phys 70:623
36. Martínez-Nuñez E, Varandas AJC (2001) J Phys Chem 105:5923
37. Takayanagi T, Kurosaki Y, Yokoyama K (2000) Chem Phys Lett 321:106
38. Jungen C, Halin K-EJ, Merer AJ (1980) Mol Phys 40:65
39. Varandas AJC (1979) J Chem Phys 70:3786

[1] For the computer code, the reader should contact the authors.